Longitudinal study of a tilt-body vehicle: modeling, control and stability analysis

Leandro R. Lustosa, François Defaÿ and Jean-Marc Moschetta[1]
Institut Supérieur de l'Aéronautique et de l'Espace,
ISAE-RESEARCH, Toulouse 31400, France

***Abstract*— This work studies a longitudinal high incidence flight envelope dynamic model for use in a convertible tilt-body vehicle designed for indoor/outdoor environments. The model assumptions are chosen so that a singularity-free nonlinear differential equation system is obtained. The model is complex enough to predict wind tunnel experiments yet simple enough to be described by analytical expressions (instead of physically difficult to interpret lookup tables). Wind tunnel measurements took place to identify flying model parameters, validate model and support autopilot design by means of scheduled linear quadratic regulator controller. Finally, controller design is validated by means of stability analysis based on regions of attraction computation via Lyapunov theorems and invariant sets during the entire transition between airplane mode and hover mode.**

I. Introduction

Remote building intrusion missions in complex urban environments calls for the use of micro air vehicles (MAVs) capable of performing both long-endurance and hover flights. Traditionally, long-endurance missions are performed by fixed-wing architectures which advantage from lift generation by aerodynamic surfaces due to the aircraft movement with respect to air. This yields high-speed stable flight even under adverse wind conditions. On the other hand, hovering platforms (e.g. multi-rotor platforms, helicopters) cannot benefit from air to vehicle relative movement and calls for energetically expensive propulsion methods that precludes long-distance missions but allows for sustained low-speed unstable indoor flights. This work proposes a hybrid architecture based on the tilt-body concept, called *MAVion* (see Fig. 1), that is capable of balancing aerodynamic and propulsion design parameters to deliver a solution to the remote building intrusion problem.

Other concepts are available for implementation in hybrid vehicles. For example, one alternative option is to tilt the engines such as in the V-22 *Osprey* configuration. One drawback in such a configuration is the appearance of aerodynamic downward forces due to propeller slipstream interaction with the wing surface. Reduction of such forces are achieved by means of tilt-wing configurations in which some fraction of the wing rotates with the rotor. In the domain of MAVs, the AVIGLE [1], the MAVerix [2] and others [3] are examples of such concept and they all require an additional engine above the horizontal tail to provide pitching moment control. Both possess moving mechanical parts that add to complexity and preclude further miniaturization but allow for fuselage horizontal stabilization during all flight stages.

The *MAVion* project philosophy is strongly based on manufacturing simplicity and transition flight capacity thus yielding a highly underactuated platform with a high degree of coupling between aerodynamic and propulsion subsystems that calls for accurate mathematical modeling, precise parameter identification and robust control laws. Previous modeling of vertical take-off and landing (VTOL) vehicles [4], [5] are used herein to support physical modeling and an aerodynamic/propulsion interaction factor k_i is introduced to abstract slipstream wake funneling effects. Furthermore, a wind tunnel campaign is performed to validate and identify all aerodynamic parameters and validate the model.

Finally, this paper shows that the highly nonlinear nature of the transition from airplane flight (stable) to hover flight (unstable) calls for nonlinear control techniques. As a first approach, this document assumes lateral stability while focusing only on longitudinal dynamics (pitch axis). A comprehensive controls overview for VTOL systems that includes proportional integral derivative (PID), pole placement, backstepping, linear-quadratic-Gaussian, H_∞ and H_2 control techniques can be found in [6]. *MAVion* employs scheduled linear quadratic regulators (LQR) to stabilize the vehicle over all trajectory and the present work contributes by means of a rigorous analysis of controller stability via invariant sets and Lyapunov candidate functions [7].

The paper is organized as follows. Section II delineates the physical and mathematical model of *MAVion* and comments

Fig. 1. *MAVion* under wind tunnel testing.

*This work was supported by the Conselho Nacional de Desenvolvimento Científico e Tecnológico, CNPq, (Brazilian National Science Foundation)

[1]{leandro-ribeiro.lustosa,francois.defay, jean-marc.moschetta}@isae-supaero.fr

over some design issues. Section III describes the process of parameter identification and the wind tunnel campaign that supported this work. Section IV portraits the control strategy adopted and rigorously prove stability for the whole hover-to-horizontal flight transition. Finally, concluding remarks and perspectives are given in section V.

II. Tilt-body longitudinal model

MAVion contains 4 moving parts with respect to the aerodynamic fuselage as Fig. 2 illustrates. Roughly, two elevons with deflections δ_1 and δ_2 deliver pitching moment (with respect to body-fixed axis $\hat{\boldsymbol{y}}_b$) and rolling moment (with respect to body-fixed axis $\hat{\boldsymbol{x}}_b$) by means of symmetrical and asymmetrical deflections, respectively, while two propeller engines with rotation speeds ω_1 and ω_2 deliver thrust and yawing moment (with respect to body-fixed axis $\hat{\boldsymbol{z}}_b$) by means of symmetrical and asymmetrical rotation speeds. Notice that is the case because the motors are installed in a counter-rotative tandem configuration with rotation direction chosen to counter wing tip vortices, which artificially increases the aspect ratio. It also provides a natural way to trigger banked turns since increasing ω_1 would not only result in a positive yaw moment but also in an induced positive rolling moment yielding a starboard curve in horizontal flight. Finally, lift is generated by the aerodynamic shape of the fuselage where inside resides most electronic parts and payload.

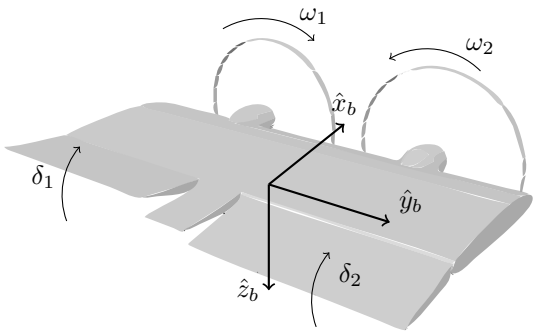

Fig. 2. Perspective view, body-axis definition and *MAVion* actuation inputs.

Figure 3 illustrates the MAVion free-body diagram during an arbitrary flight instant. We assume symmetry in counter-rotating propellers speed ω and elevons deflection δ to cancel out lateral/directional dynamics and focus on longitudinal flight. Under these assumptions, convenient system state $\boldsymbol{x}'$, actuator $\boldsymbol{u}$ and disturbance $\boldsymbol{w}$ definitions are

$$\boldsymbol{x}' = \begin{pmatrix} v_n \\ v_d \\ \theta \\ \dot{\theta} \end{pmatrix}, \quad \boldsymbol{u} = \begin{pmatrix} \omega \\ \delta \end{pmatrix}, \quad \boldsymbol{w} = \begin{pmatrix} w_n \\ w_d \end{pmatrix} \tag{1}$$

where v_n, v_d, w_n, w_d and θ, denote, respectively, MAVion and wind velocities with respect to the ground expressed in the local north-east-down (NED) coordinate system, and pitch angle with respect to the local horizontal.

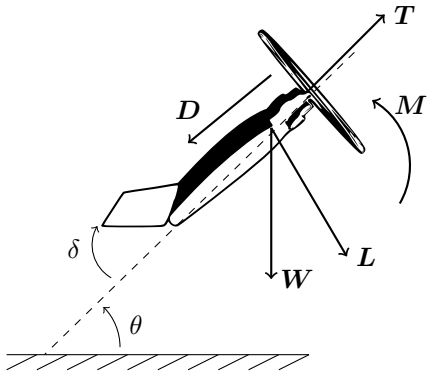

Fig. 3. *MAVion* free-body diagram: aerodynamic/propulsion forces and moments conventions and directions.

In order to calculate $\dot{\boldsymbol{x}}'$, we apply Newton's second law (see Fig. 3) and obtain

$$m\dot{v}_n = (D + 2T)cos\theta + Lsin\theta \tag{2}$$

$$m\dot{v}_d = mg + Lcos\theta - (2T + D)sin\theta \tag{3}$$

$$J_y\ddot{\theta} = M \tag{4}$$

where g, m and J_y denote, respectively, local gravity, MAVion mass and inertia moment with respect to the y-axis. Notice that, otherwise stated, aerodynamic drag D and lift L, aerodynamic pitching moment M, and propulsion thrust T are hereafter described in body-fixed axes.

A. Aerodynamic model

By means of the Buckingham-Π theorem [8] and assuming inviscid incompressible flow, we relate the aerodynamic forces and moments to the system state according to

$$L = \frac{1}{2}\rho v_\infty^2 S C_L(\alpha, \delta) \tag{5}$$

$$D = \frac{1}{2}\rho v_\infty^2 S C_D(\alpha, \delta) \tag{6}$$

$$M = \frac{1}{2}\rho v_\infty^2 \bar{c} S C_M(\alpha, \delta) \tag{7}$$

where ρ, v_∞, S, $\bar{c}$, α, C_L, C_D and C_M are, respectively, air density at drone location, true air speed with respect to the drone, reference wing area and chord, angle of attack; and lift, drag and pitching moment coefficients. Furthermore, for a fixed $\delta = \delta_0$, the wide envelope of flight angles precludes the use of a linear aerodynamics coefficient model and calls for a Fourier series 2π-periodic function approximation such as

$$C_L(\alpha, \delta_0) = A_{L0}(\delta_0) + \sum_{k=1}^{N} A_{Lk}(\delta_0)cos\alpha + B_{Lk}(\delta_0)sin\alpha \tag{8}$$

As it will be presently shown, the choice of picking only the $k = 2$ term for moment terms and $k = 1$ for force terms yields a non-linear differential equation structure which has good properties we shall take advantage in the analysis and design phase. On the other hand, we model the effect of

elevon deflection on $C_L(\alpha,\delta)$, $C_D(\alpha,\delta)$ and $C_M(\alpha,\delta)$ as a linear extra term in α. Mathematically,

$$C_L(\alpha,\delta) = A_{L0} + A_{L1}cos(\alpha) + B_{L1}sin(\alpha) + C_{L\delta}\delta \quad (9)$$

$$C_D(\alpha,\delta) = A_{D0} + A_{D1}cos(\alpha) + B_{D1}sin(\alpha) + C_{D\delta}\delta \quad (10)$$

$$C_M(\alpha,\delta) = A_{M0} + A_{M2}cos(2\alpha) + B_{M2}sin(2\alpha) + C_{M\delta}\delta \quad (11)$$

which yields

$$C_M(\alpha,\delta) = C_{Ma} + C_{Mb}cos^2\alpha + C_{Mc}sin\alpha cos\alpha + C_{M\delta}\delta \quad (12)$$

for the following change of parameters

$$\begin{pmatrix} C_{Ma} \\ C_{Mb} \\ C_{Mc} \end{pmatrix} = \begin{bmatrix} 1 & -1 & 0 \\ 0 & 2 & 0 \\ 0 & 0 & 2 \end{bmatrix} \begin{pmatrix} A_{M0} \\ A_{M2} \\ B_{M2} \end{pmatrix} \quad (13)$$

Furthermore, notice that

$$\begin{pmatrix} cos\alpha \\ sin\alpha \end{pmatrix} = \frac{-1}{v_\infty} \begin{bmatrix} cos\theta & -sin\theta \\ sin\theta & cos\theta \end{bmatrix} \begin{pmatrix} w_n - v_n \\ w_d - v_d \end{pmatrix} \quad (14)$$

The discontinuity at the origin in equation 14 does not pose a problem for fixed-wings since they operate always with $v_\infty >> 0$. However, hovering vehicles ideally operate exactly at the discontinuity position and call for a different parametrization that bypass α. By substituting equations 12 and 14 into equation 7, for instance, we obtain

$$M = p_m(\boldsymbol{x}', \boldsymbol{u}, \boldsymbol{w}, cos\theta, sin\theta) \quad (15)$$

where $p_m(\cdot)$ is a nonlinear function of the listed arguments and has an analytical expression that does not include α, and it is thus more suitable to model and numerically simulate hovering flight. To transform it into a more numerically stable non-trigonometric function of only $\boldsymbol{x}'$, $\boldsymbol{u}$ and $\boldsymbol{w}$, we can use the quaternion formulation, which for longitudinal flight yields

$$\boldsymbol{q} = \begin{pmatrix} q_0 \\ q_1 \\ q_2 \\ q_3 \end{pmatrix} = \begin{pmatrix} cos(\frac{\theta}{2}) \\ 0 \\ sin(\frac{\theta}{2}) \\ 0 \end{pmatrix} \quad (16)$$

From the double arc angle formula we obtain the relation between Euler angles and quaternion formulation.

$$cos\theta = cos^2(\frac{\theta}{2}) - sin^2(\frac{\theta}{2}) = q_0^2 - q_2^2 \quad (17)$$

$$sin\theta = 2sin(\frac{\theta}{2})cos(\frac{\theta}{2}) = 2q_0q_2 \quad (18)$$

We substitute above results into equation 15 and redefine the state $\boldsymbol{x}'$ to be

$$\boldsymbol{x} = \begin{pmatrix} v_n & v_d & q_0 & q_2 & \dot{\theta} \end{pmatrix}^T \quad (19)$$

so that we obtain a nonlinear equation on $\boldsymbol{x}$, $\boldsymbol{u}$ and $\boldsymbol{w}$ only (equation 20). A similar development is performed on aerodynamic drag and lift forces counterparts to obtain non-trigonometric equations for D and M (equations 21 and 22).

$$L = p_l(\boldsymbol{x}, \boldsymbol{u}, \boldsymbol{w}) \quad (20)$$

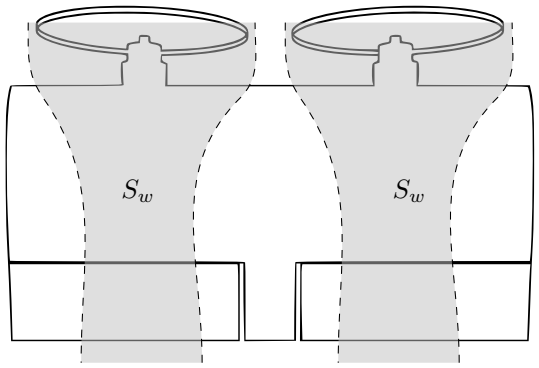

Fig. 4. Propeller wing interaction: slipstream wake illustration and the division between dry and wet sections.

$$D = p_d(\boldsymbol{x}, \boldsymbol{u}, \boldsymbol{w}) \quad (21)$$

$$M = p_m(\boldsymbol{x}, \boldsymbol{u}, \boldsymbol{w}) \quad (22)$$

B. Propulsion model

Similarly to the aerodynamic forces and moments development, an argument by means of the Buckingham-Π theorem yields

$$T = \rho\omega^2 D_p^4 C_T(J) \quad (23)$$

where D_p, C_T and J are, respectively, propeller reference diameter, thrust coefficient and advance ratio given by

$$J = \frac{v_\infty cos\alpha}{\omega D_p} \quad (24)$$

In high angle of attack flight, the thrust coefficient is commonly modeled [4] as

$$C_T(J) = C_{T0} + C_{TJ}J \quad (25)$$

Notice that we don't model propeller external torques due to the counter-rotating propellers and longitudinal motion assumptions. Finally, we substitute equations 14, 17, 18, 24 and 25 into 23 to obtain the following polynomial equation

$$T = p_t(\boldsymbol{x}, \boldsymbol{u}, \boldsymbol{w}) = C_{T0}\rho\omega^2 D_p^4 + \\ + \rho\omega D_p^3 C_{TJ}\Big((q_0^2 - q_2^2)(v_n - w_n) + 2q_0q_2(w_d - v_d)\Big) \quad (26)$$

C. Wing-propeller interaction

The development of the aerodynamic forces model assumed that the free-stream relative wind velocity is independent of the propulsion system. One could design a propulsion system to deliver low wake induced velocity to attain to this assumption. However, under this assumption, hovering flight would deliver zero free-stream velocity and consequently zero aerodynamic forces and moments that would preclude attitude control. Therefore, slip-stream air induced velocity is a design quantity that must be not reduced, but instead, kept in a interval of acceptable and influential values posing an additional design challenge in comparison to flying wings. An appropriate model is therefore necessary and described in the following.

We follow the guidelines settled in [9] and define two different wing sections as illustrated by Fig. 4. We assume one of them to be unaffected by the propulsion wake and is modeled according to equations 20, 21 and 22. The other will be affected by a slip-stream wake profile and its effect on the aerodynamic equations is modeled by means of a induced free-stream velocity $\boldsymbol{v}_{\infty,i}$ and an accordingly induced angle of attack α_i as illustrated by figure 5. The geometry of the model suggests superposition over the air flows and the following modification in the angle of attack equation (see equation 14)

$$\begin{pmatrix} cos\alpha_i \\ sin\alpha_i \end{pmatrix} = \frac{-1}{v_{\infty,i}} \left(\begin{bmatrix} cos\theta & -sin\theta \\ sin\theta & cos\theta \end{bmatrix} \begin{pmatrix} w_n - v_n \\ w_d - v_d \end{pmatrix} - \begin{pmatrix} v_i \\ 0 \end{pmatrix} \right) \tag{27}$$

where v_i is the induced velocity of slip-stream at the downstream side of propeller disk which, by means of the propeller momentum theory for forward helicopter flight [10], is a solution of

$$v_i^2 + v_\infty cos\alpha v_i - \frac{T}{2\rho S_p} = 0 \tag{28}$$

where S_p denotes propeller disk area. Therefore, we write

$$v_i = \frac{1}{2}\left[\sqrt{(v_\infty cos\alpha)^2 + \frac{2T}{\rho S_p}} - v_\infty cos\alpha \right] \tag{29}$$

where the α-based terms can be again passed-by by substitution of equation 14. Notice also that equation 27 yields

$$\begin{aligned} v_{\infty,i}^2 &= (w_n - v_n)^2 + (w_d - v_d)^2 + v_i^2 + \cdots \\ &\cdots + 2v_i\Big((q_0^2 - q_2^2)(v_n - w_n) - 2q_0 q_2 (v_d - w_d) \Big) \end{aligned} \tag{30}$$

Finally, for aerodynamic forces and moments in the slip-stream area we have

$$L_w = \frac{1}{2}\rho v_{\infty,i}^2 S_w C_L(\alpha_i, \delta) \tag{31}$$

$$D_w = \frac{1}{2}\rho v_{\infty,i}^2 S_w C_D(\alpha_i, \delta) \tag{32}$$

$$M_w = \frac{1}{2}\rho v_{\infty,i}^2 \bar{c} S_w C_M(\alpha_i, \delta) \tag{33}$$

where S_w denotes the wet area of the wing. In this work, we shall model it as (see Fig. 4)

$$S_w = \bar{c} D_p \tag{34}$$

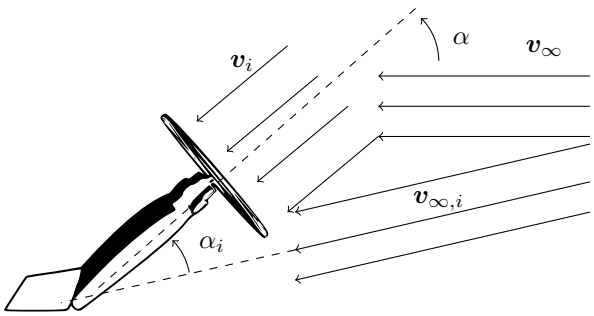

Fig. 5. Computation of induced relative air velocity $\boldsymbol{v}_{\infty,i}$ and induced angle of attack α_i by means of superposition of flows assumption.

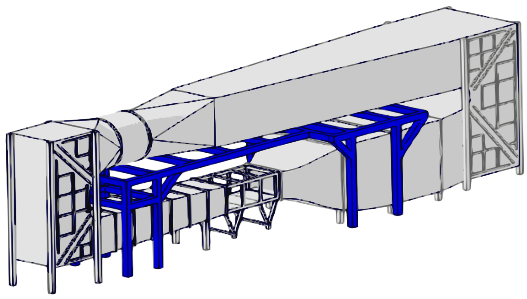

Fig. 6. SabRe (*Soufflerie bas Reynolds*) closed-loop wind tunnel facility.

and

$$S_d = S - 2S_w \tag{35}$$

However, in the light of the moment theory [4] one can show that the wet area S_w contracts before it reaches the elevons and that v_i changes along the slipstream direction. These phenomena are hard to model in the presence of a aerodynamic surface in the propeller wake thus we introduce in this work the factor k_i in equation 29 to take these effects into account by modifying the induced velocity v_i such that

$$v_i = \frac{k_i}{2}\left[\sqrt{(v_\infty cos\alpha)^2 + \frac{2T}{\rho S_p}} - v_\infty cos\alpha \right] \tag{36}$$

The interaction factor k_i should be tunned by means of experimental data or computer fluid dynamics software. Finally, substitution of equations 12 and 27 into 31, 32 and 33 yields nonlinear equations of the form of equations 37, 38 and 39.

$$L_w = p_{l,w}(\boldsymbol{x}, \boldsymbol{u}, \boldsymbol{w}) \tag{37}$$

$$D_w = p_{d,w}(\boldsymbol{x}, \boldsymbol{u}, \boldsymbol{w}) \tag{38}$$

$$M_w = p_{m,w}(\boldsymbol{x}, \boldsymbol{u}, \boldsymbol{w}) \tag{39}$$

D. Putting it all together

The dynamic equations can then be written as

$$\dot{\boldsymbol{x}} = f(\boldsymbol{x}, \boldsymbol{u}, \boldsymbol{w}) \tag{40}$$

where $f : \mathbb{R}^9 \to \mathbb{R}^5$ is a nonlinear, non-trigonometric and singularity-free function for all values normally encountered in all stages of flight.

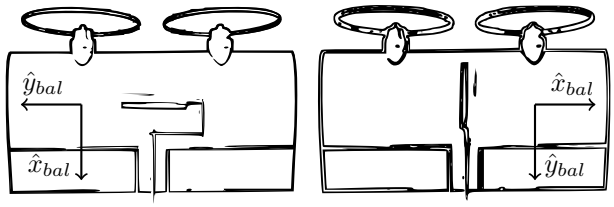

Fig. 7. Two internal balance configurations.

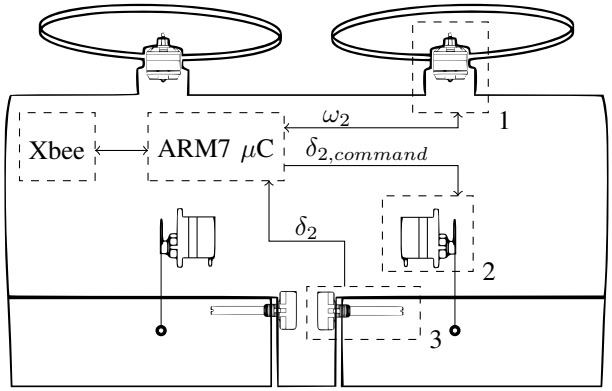

Fig. 8. MAVion wind tunnel model instrumentation.

III. Parameters identification and fixed points

The mathematical model provides the means to exploit isolated aerodynamic and propulsion data and predict the behavior of the whole vehicle and reason over its design features (e.g., mass, airfoil, propeller geometry). Therefore, except for k_i, the mathematical model parameters are either pure geometric, aerodynamic or propulsion quantities and can be identified separately.

While geometric quantities can be directly measured, aerodynamic and propulsion coefficients call for wind tunnel measurements. For the sake of completeness, this section superficially describes the wind tunnel campaign that supported this work (see [11] for more information) and how the longitudinal subset of the collected data was used to interpolate the aerodynamic coefficients, tune the interaction factor k_i and validate the model. Propulsion identification was carried out in [12] and the respective parameters (among all others identified in this work) can be found in the appendix section.

The experiments were ran at the SabRe closed-loop wind tunnel (Fig. 6) located at ISAE and capable of delivering low Reynolds stable and uniform flow at a wind velocity range of 2 to 25 m/s, thus ideal for experimenting full-span micro

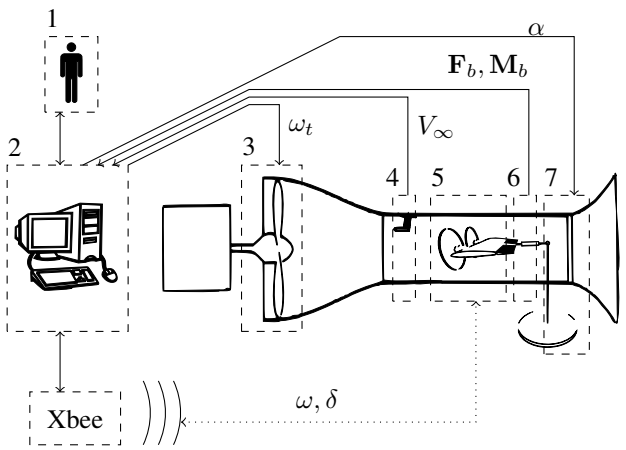

Fig. 9. Wind tunnel acquisition system set-up.

air vehicles. Although a 6-component study was performed (3-dimensional forces and moments), this paper focus only on longitudinal quantities, i.e., drag $\boldsymbol{D}$, lift $\boldsymbol{L}$ and pitching moment $\boldsymbol{M}$ measured with zero sideslip. Forces and moments were measured by means of a calibrated 5-component internal balance in two different configurations (see figure 7) in order to obtain the 6 force/moment components (see [11] for more information).

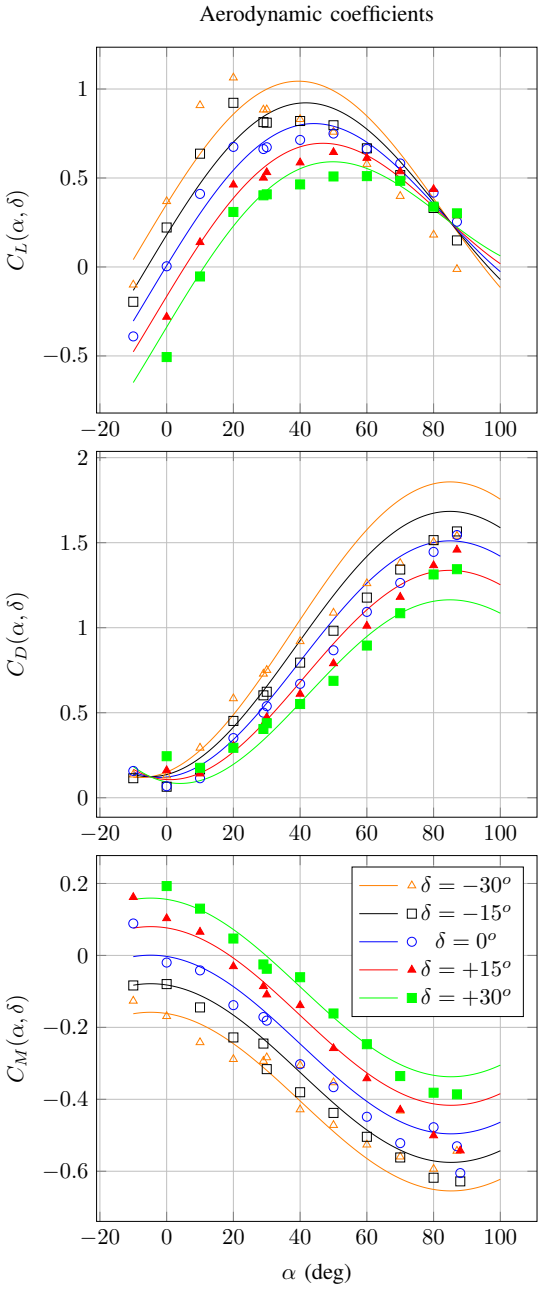

Fig. 10. LMS interpolated curves (solid lines) of the measured data (marks).

An adapted MAVion was manufactured for wind tunnel campaign purposes (Fig. 1). Its main objectives were to enable rigid installment of the internal balance in both configurations and to provide a non-deformable airfoil section to aerodynamic identification. Fig. 8 illustrates the electronic

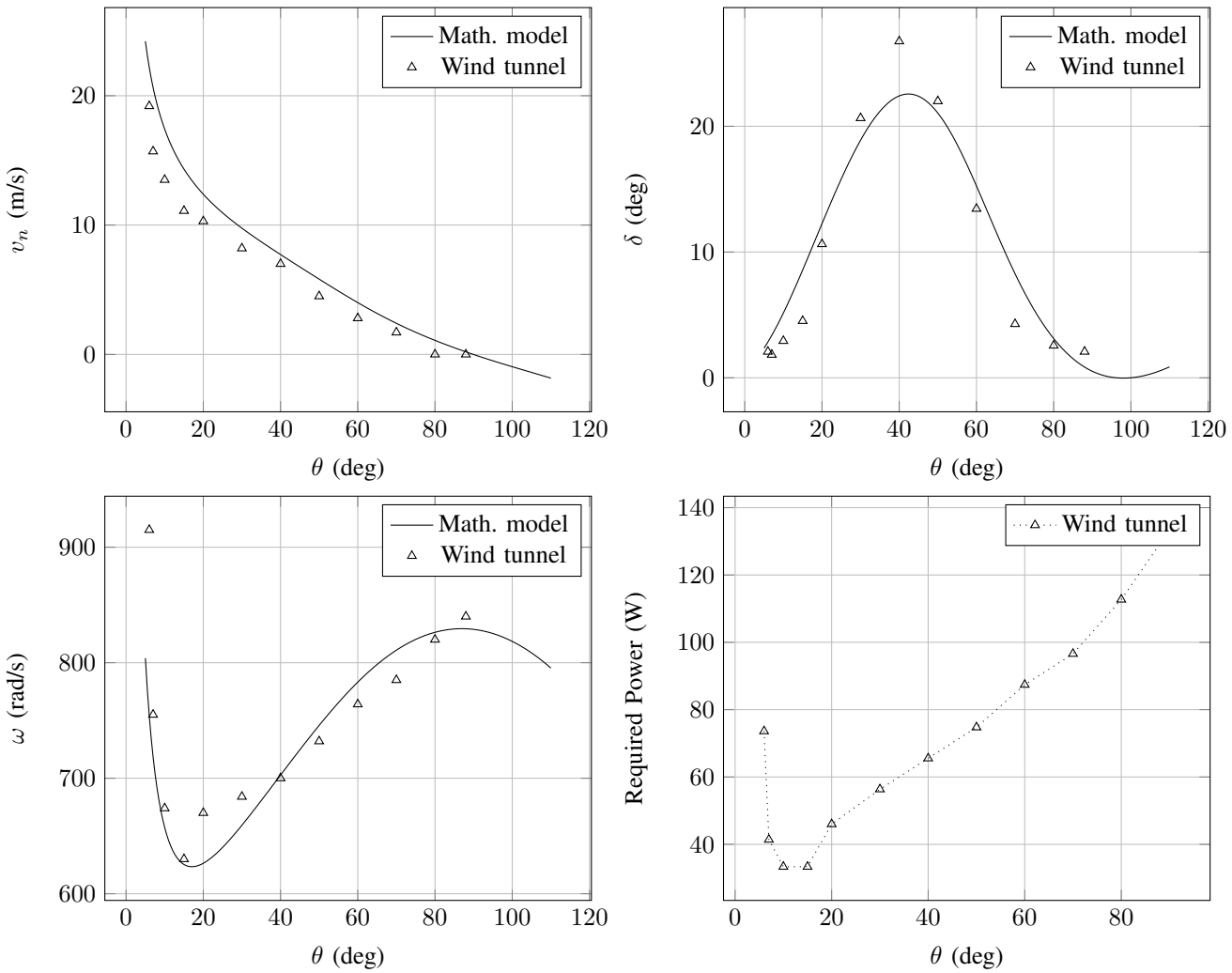

Fig. 11. Required velocity v_n, elevon deflection δ, propeller speed ω and power P for achieving equilibrium at a given pitch angle θ. Notice that the mathematical model does not model power requirements thus there is no model fixed points in the required power figure. Furthermore, power was estimated by measuring the electric current into the system and accounts for motors, electronics, propellers engines and *XBee* radio transmission link.

counterpart. Notice that elevon deflections were measured by means of potentiometers installed directly at the elevons avoiding servo measurements that are susceptible to inaccuracy due to rod deformations and servo-control errors. On the other hand, propellers speed were measured by the brushless CC motors speed controllers.

The campaign data set is roughly divided in two parts. The first was taken by independently setting the angle of attack α, motor speed ω and flap deflection δ to the values illustrated by table I. All combinations were exhaustively explored and the associated forces and moments registered. Notice that the unconventional nature of the vehicle calls for an unconventional envelope of testing variables that include very high angles of incidence. Fig. 10 isolates aerodynamic data from propulsion data by plotting the experimental aerodynamic coefficients in the wind coordinate system for $\omega = 0$ and different elevon deflections. Each coefficient point is calculated by means of equations 5, 6 or 7, and later interpolated by least mean-squares to fit equations 9, 10 and 11. The results are shown in Fig. 10.

The second data set comprises of wind relative velocity, elevon deflection and propeller rotation required to achieve static equilibrium in a given angle of attack. The experimental procedure fundamental idea is to, as previously done in [13], for each sampled α, iteratively search for values V_∞, δ_i, ω_i that will deliver aerodynamic/propulsion forces and moments (notice gravitational suppression) that will cancel gravitational forces and moments on the *flying* model; which has a different mass distribution than the wind tunnel model that is not meant to fly.

V_∞	10	m/s
α	$-10, 0, 10, 20, 30, 40, 50, 60, 70, 80, 90$	deg
ω	$0, 400, 800$	rad/s
δ	$-30, -15, 0, 15, 30$	deg

TABLE I

FLIGHT VARIABLES TESTED IN LONGITUDINAL CONFIGURATION.

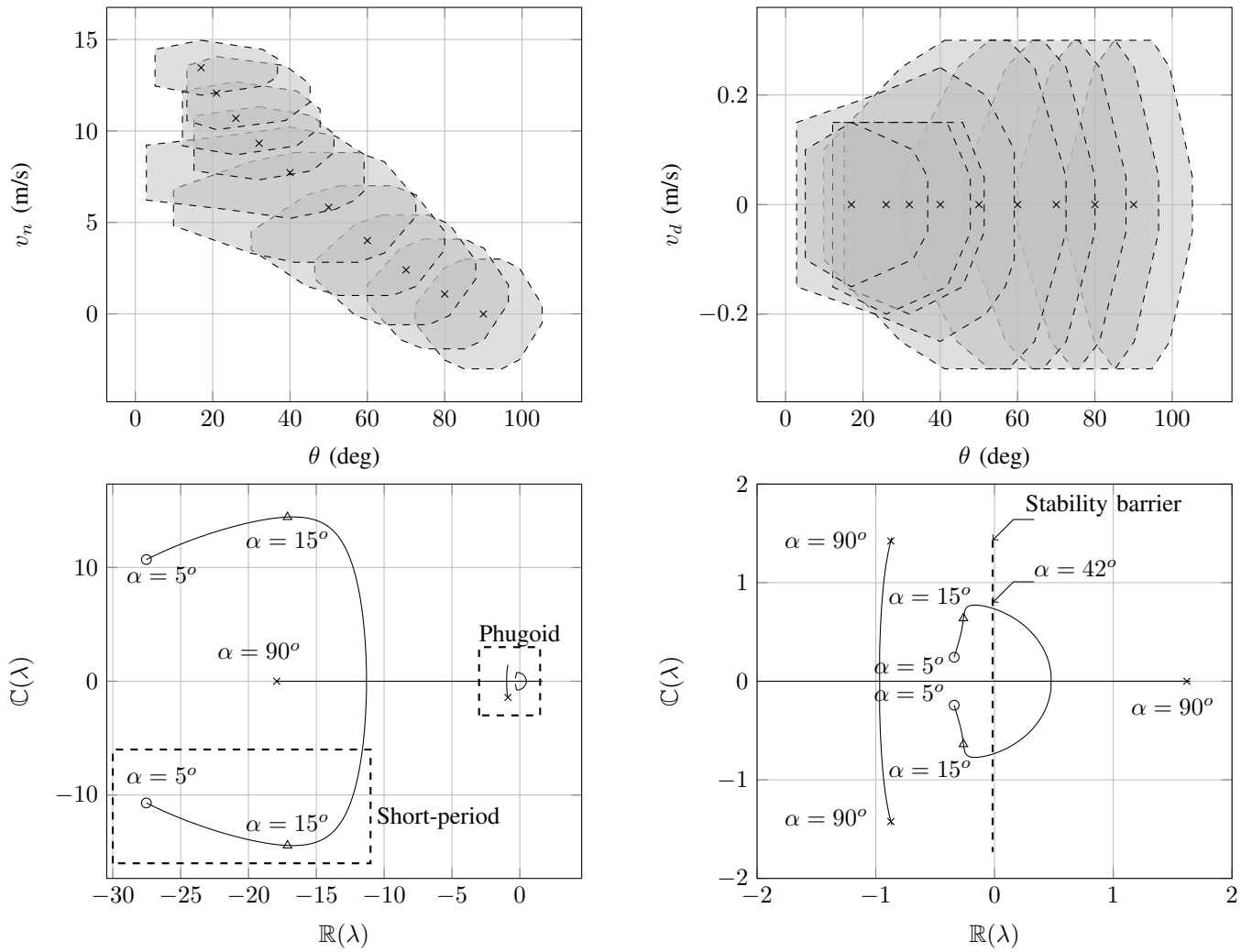

Fig. 12. Top left and right: regions of attraction for scheduled LQR controller during equilibrium transition for v_n and v_d, respectively. Bottom left: poles movement of the open-loop transition matrix A along the equilibrium transition trajectory. Bottom right: zoomed-in phugoid region.

The desired flying model mass distribution is such that the center of mass is longitudinally located at a position $0.15c$ away from the leading edge and is motivated by a 10% stability margin controls requirement. The results can be seen in Fig. 11 along with power required curves. Furthermore, at this stage, all mathematical model parameters are identified except k_i which is determined by

$$k_i = \arg\min_{k_i} \sum_{j=1}^{N_p} f(\boldsymbol{x}_j, \boldsymbol{u}_j, \mathbf{0})^T S f(\boldsymbol{x}_j, \boldsymbol{u}_j, \mathbf{0}) \tag{41}$$

where

$$\boldsymbol{x}_j = \begin{pmatrix} v_{n,j} & 0 & cos(\frac{\alpha_j}{2}) & sin(\frac{\alpha_j}{2}) & 0 \end{pmatrix}^T \tag{42}$$

and

$$\boldsymbol{u}_j = \begin{pmatrix} \delta_j & \omega_j \end{pmatrix}^T \tag{43}$$

where N_p is the number of experimental points, $\{v_{n,j}, \delta_j, \omega_j\}$ are the experimental equilibrium variables for a given α_j, and S is a diagonal positive definite scaling matrix to account for different orders of magnitude between $f(\cdot)$ components. Finally, after identifying k_i, the mathematical equilibrium curves can be plotted by means of numerically solving $f(\boldsymbol{x}, \boldsymbol{u}, \mathbf{0}) = 0$ and compared with experimental values for model validation. The results can be seen on Fig. 11.

The results validate the design by demonstrating that the *MAVion* is capable of sustaining flight from 0m/s to 20m/s in the absence of wind. Equivalently speaking, the *MAVion* is capable of maintaining hover flight in adverse wind conditions up to 20m/s. It is noted that *MAVion* maximum speed was not reached in wind tunnel testing due to internal balance strain gauge saturation and it is still an unknown. However, the blow-up in propeller engine rotation ω for small angles of attack in the equilibrium figures suggests an upper bound of $v_n \leq 20$m/s. Finally, the elevator deflection angle shows a maximum of $\delta = 27^o$ at $\alpha = 40^o$, within the range of the elevon aerodynamic efficiency. This confirms that the propeller slipstream is strong enough to guarantee pitch control throughout the entire transition flight.

Finally, the mathematical model allows for drag polar computation (see Fig. 14) which defines the necessary angle

Require: $Q, R > 0$ for acceptable hover flight performance
Require: $\rho_{init} > 0, \Delta\rho > 0$
  $i \leftarrow 0$
  $(\boldsymbol{x}_i, \boldsymbol{u}_i) \leftarrow (\boldsymbol{x}_h, \boldsymbol{u}_h)$
  while $\exists p \in \mathbb{F} : p \notin \cup_{k=0}^{i} R(\rho_k)$ **do**
    $i \leftarrow i + 1$
    $\rho \leftarrow \rho_{init}$
    $A \leftarrow \frac{\partial f}{\partial \boldsymbol{x}}\Big|_{\boldsymbol{x}=\boldsymbol{x}_0, \boldsymbol{u}=\boldsymbol{u}_0}$, $B \leftarrow \frac{\partial f}{\partial \boldsymbol{u}}\Big|_{\boldsymbol{x}=\boldsymbol{x}_0, \boldsymbol{u}=\boldsymbol{u}_0}$
    Compute LQR gain K_i for linear system $\dot{\tilde{\boldsymbol{x}}} = A\tilde{\boldsymbol{x}} + B\tilde{\boldsymbol{u}}$
    while $\dot{\boldsymbol{x}}^T P\tilde{\boldsymbol{x}} + \tilde{\boldsymbol{x}}^T P\dot{\boldsymbol{x}} < 0 \quad \forall \tilde{\boldsymbol{x}} : V(\tilde{\boldsymbol{x}}) < \rho + \Delta\rho$ **do**
      $\rho \leftarrow \rho + \Delta\rho$
    end while
    $\rho_i \leftarrow \rho$
    Find $(\boldsymbol{x}^*, \boldsymbol{u}^*) \in \mathbb{F} : (\boldsymbol{x}^* - \boldsymbol{x}_i)^T P(\boldsymbol{x}^* - \boldsymbol{x}_i) = 0.70\rho_i$
    $(\boldsymbol{x}_{i+1}, \boldsymbol{u}_{i+1}) \leftarrow (\boldsymbol{x}^*, \boldsymbol{u}^*)$
  end while

Fig. 13. Summary of equilibrium trajectory fixed point sampling and global scheduled LQR controller generation algorithm.

of attack α_h (and consequently $\boldsymbol{x}_h$ and $\boldsymbol{u}_h$) for maximum endurance. Such point will be defined as MAVion's horizontal flight cruise equilibrium point. On the other hand, the point where $v_n = 0$, i.e. hover equilibrium points $\boldsymbol{x}_v$ and $\boldsymbol{u}_v$, can be as well easily computed and both valors are illustrated at table II among other flight quantities that derives from the results from this section.

IV. Control design and stability analysis

For the purpose of assessing local stability of an equilibrium point $(\boldsymbol{x}_0, \boldsymbol{u}_0, \boldsymbol{0})$, consider the following linearization of $f(\boldsymbol{x}, \boldsymbol{u}, \boldsymbol{0})$

$$\dot{\boldsymbol{x}} = f(\boldsymbol{x}, \boldsymbol{u}, \boldsymbol{0}) \approx A\tilde{\boldsymbol{x}} + B\tilde{\boldsymbol{u}} \tag{44}$$

where

$$A = \frac{\partial f}{\partial \boldsymbol{x}}\bigg|_{\substack{\boldsymbol{x}=\boldsymbol{x}_0 \\ \boldsymbol{u}=\boldsymbol{u}_0}}, \quad B = \frac{\partial f}{\partial \boldsymbol{u}}\bigg|_{\substack{\boldsymbol{x}=\boldsymbol{x}_0 \\ \boldsymbol{u}=\boldsymbol{u}_0}} \tag{45}$$

and

$$\tilde{\boldsymbol{x}} = \boldsymbol{x} - \boldsymbol{x}_0, \quad \tilde{\boldsymbol{u}} = \boldsymbol{u} - \boldsymbol{u}_0 \tag{46}$$

Fig. 12 shows the poles of the open-loop transition matrix A along the fixed point curves previously shown in Fig. 11. It can be readily seen that the MAVion is longitudinally stable during horizontal flight for values of θ as high as 42^o. After this value, MAVion operates in unstable fixed points that calls for nonlinear control techniques. Additionally, traditional short-period and phugoid fixed-wing aircraft dynamics can be exploited from the figure. For instance, for horizontal cruise flight ($\alpha = 15^o$), *MAVion* experiences a reasonable well damped ($\xi = 0.76$) short-period mode with period $T = 0.44$ seconds that would be acceptable to human pilots. Additionally, the phugoid mode delivers a more lightly damped ($\xi = 0.40$) oscillation that can still be compensated out due to its large period: $T = 9.84$ seconds.

Angle of attack for hovering	$\alpha_v = 90^o$
Angle of attack for horizontal flight	$\alpha_h = 15^o$
Maximum speed under good weather	20m/s
Maximum wind rejection under hover	20m/s
Cruise speed	12m/s
Maximum endurance	40min
Endurance in hover	10min

TABLE II
Estimated flight quantities assuming a 50g camera payload.

The control technique employed herein to stabilize MAVion during the horizontal-to-hover trajectory made up of its fixed points is gain-scheduled linear quadratic regulator (LQR) [14], [15], [16], [17]. This strategy computes the linear controller $\tilde{\boldsymbol{u}} = -K\tilde{\boldsymbol{x}}$ that minimizes the following quadratic cost function:

$$J(\tilde{\boldsymbol{u}}) = \int_0^\infty (\tilde{\boldsymbol{x}}^T Q\tilde{\boldsymbol{x}} + \tilde{\boldsymbol{u}}^T R\tilde{\boldsymbol{u}})dt \tag{47}$$

subject to the linearized system dynamics of Eq. 44 at a fixed point $(\boldsymbol{x}_i, \boldsymbol{u}_i)$. In this way, it is possible to transition from one fixed point $(\boldsymbol{x}_i, \boldsymbol{u}_i)$ to another close-by fixed point $(\boldsymbol{x}_{i+1}, \boldsymbol{u}_{i+1})$ by means of a linear controller. A sequence of such steps yields the global controller necessary to take the MAVion from horizontal flight equilibrium point at $(\boldsymbol{x}_h, \boldsymbol{u}_h)$ to hover flight equilibrium point at $(\boldsymbol{x}_v, \boldsymbol{u}_v)$.

The question that remains is how many equilibrium points (and therefore different LQR controllers) are necessary to cover the whole transition. For that, the region of attraction of fixed points and the trajectory are simultaneously calculated by means of Lyapunov level sets [7] according to the Algorithm 13. The algorithm basically starts from one equilibrium point $(\boldsymbol{x}_i, \boldsymbol{u}_i)$ and attempt to prove its asymptotic stability in the largest region $R(\rho)$ of the form

$$R(\rho) = \{\tilde{\boldsymbol{x}} \in \mathbb{R}^5 : V(\tilde{\boldsymbol{x}}) < \rho\} \tag{48}$$

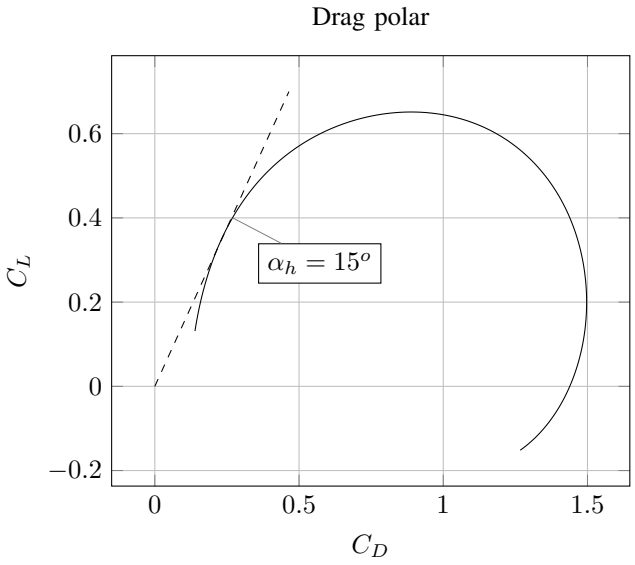

Fig. 14. Aerodynamic drag polar and max endurance operating point.

by means of a Lyapunov candidate function of the form

$$V(\tilde{\boldsymbol{x}}) = \tilde{\boldsymbol{x}}^T P \tilde{\boldsymbol{x}} \tag{49}$$

for some positive definite P. For that to happen, the function $V(\tilde{\boldsymbol{x}})$ must respect

$$\dot{V}(\tilde{\boldsymbol{x}}) = \dot{\boldsymbol{x}}^T P \tilde{\boldsymbol{x}} + \tilde{\boldsymbol{x}}^T P \dot{\boldsymbol{x}} < 0 \quad \forall \tilde{\boldsymbol{x}} \in \mathbb{R}^5 : V(\tilde{\boldsymbol{x}}) < \rho \tag{50}$$

where

$$\dot{\boldsymbol{x}} = f(\boldsymbol{x}, -K\tilde{\boldsymbol{x}}, \mathbf{0}) \tag{51}$$

The largest ρ that satisfies equation 50 for a fixed point $(\boldsymbol{x}_i, \boldsymbol{u}_i)$ is denoted ρ_i. Given $R(\rho_i)$, the next fixed point $(\boldsymbol{x}_{i+1}, \boldsymbol{u}_{i+1})$ is chosen such that it is inside the region of attraction of $(\boldsymbol{x}_i, \boldsymbol{u}_i)$. For robustness, this work chooses $(\boldsymbol{x}_{i+1}, \boldsymbol{u}_{i+1}) \in \mathbb{F}$ ($\mathbb{F}$ is defined hereafter as the set of all equilibrium points in the horizontal-to-hover trajectory defined in Fig. 11) such that

$$V(\boldsymbol{x}_{i+1} - \boldsymbol{x}_i) = (\boldsymbol{x}_{i+1} - \boldsymbol{x}_i)^T P (\boldsymbol{x}_{i+1} - \boldsymbol{x}_i) = 0.70\rho_i \tag{52}$$

The procedure is summarized in Fig. 13 and yields the regions of attraction illustrated by Fig. 12. It proves stability for the scheduled LQR controller during the entire transition flight if a minimum of 10 trim points are correctly chosen. Since stability demonstrations by means of Lyapunov functions deliver only sufficient conditions, it could be the case that less trim points were necessary. Furthermore, the figure additionally serves as a flight envelope which guarantees stability during any longitudinal flight using this controller.

V. Conclusion

A longitudinal study of a tilt-body vehicle called *MAVion* was conducted and included modeling, identification of parameters and design of a nonlinear controller to allow for flight stability over all longitudinal flight envelope.

Aerodynamic coefficients were identified by means of a wind tunnel campaign and the mathematical model accurately predicted an equilibrium transition trajectory. Wind tunnel data confirmed a maximum speed under good weather of 20m/s and hover flight stability under adverse wind conditions up to 20m/s. In the light of this results, *MAVion* proved to be a good platform for outdoors not only because of its horizontal flight mode but also for its good wind rejection feature.

The study of the dynamic behavior described how stable fixed-wing aircraft phugoid dynamic modes turn into unstable modes by studying the movement of linearized system poles during an equilibrium trajectory. Furthermore, a Lyapunov stability analysis took place to discover a sufficient number of trim points to ensure controller stability. Finally, the lateral/directional dynamics have to be studied for outdoor flight under windy conditions to ensure that the MAVion can follow a complex trajectory.

Acknowledgment

The authors gratefully acknowledge the Conselho Nacional de Desenvolvimento Científico e Tecnológico, CNPq, (Brazilian National Science Foundation), for partial financial support for this work through the "Ciência sem Fronteiras" program.

References

[1] J. Holsten, T. Ostermann, and D. Moormann, "Design and wind tunnel tests of a tiltwing UAV," *CEAS Aeronautical Journal*, vol. 2, no. 1-4, pp. 69–79, 2011.

[2] M. Schutt, P. Hartmann, and D. Moormann, "Fullscale windtunnel investigation of actuator effectiveness during stationary flight within the entire flight envelope of a tiltwing MAV," in *IMAV 2014: International Micro Air Vehicle Conference and Competition*, 2014.

[3] D. A. Ta, I. Fantoni, and R. Lozano, "Modeling and control of a tilt tri-rotor airplane," in *American Control Conference*, 2012.

[4] B. W. McCormick, *Aerodynamics of V/STOL flight*. Dover publications, 1998.

[5] A. Vuruskan, B. Yuksek, U. Ozdemir, A. Yukselen, and G. Inalhan, "Dynamic modeling of a fixed-wing VTOL UAV," in *2014 International Conference on Unmanned Aircraft Systems*, 2014.

[6] M.-D. Hua, T. Hamel, P. Morin, and C. Samson, "Introduction to feedback control of underactuated VTOL vehicles: a review of basic control design ideas and principles," *IEEE Control Systems*, vol. 33, no. 1, pp. 61–75, 2013.

[7] G. Valmorbida and J. Anderson, "Region of attraction via invariant sets," in *2014 American Control Conference*, 2014.

[8] J. D. Anderson, *Fundamentals of aerodynamics*. McGraw-Hill, 2001.

[9] Y. Ameho, *Du pilotage d'une famille de drones a celui d'un drone hybride via la commande adaptative*. PhD thesis, Institut Superieur de l'Aeronautique et de l'Espace, 2013.

[10] J. G. Leishman, *Principles of helicopter aerodynamics*. Cambridge University Press, 2006.

[11] L. R. Lustosa, F. Defay, and J. M. Moschetta, "Development of the flight model of a tilt-body MAV," in *IMAV 2014 International Micro Air Vehicle conference and competition*, 2014.

[12] M. P. Merchant and L. S. Miller, "Propeller performance measurement for low Reynolds number UAV applications," in *44th AIAA Aerospace Sciences Meeting and Exhibit*, 2006.

[13] M. Itasse, J. M. Moschetta, Y. Ameho, and R. Carr, "Equilibrium transition study for a hybrid MAV," *International Journal of Micro Air Vehicles*, vol. 3, pp. 229–245, december 2011.

[14] W. B. Dunbar and R. M. Murray, "Model predictive control of a thrust-vectored flight control experiment," in *2002 IFAC World Congress*, 2002.

[15] I. Masar and E.Stohr, "Gain-scheduled LQR-control for an autonomous airship," in *18th International Conference on Process Control*, 2011.

[16] A. Halder, K. Lee, and R. Bhattacharya, "Probabilistic robustness analysis of F-16 controller performance: an optimal transport approach," in *2013 American Control Conference*, 2013.

[17] E. Reyes-Valeria, R. Enriquez-Caldera, S. Camacho-Lara, and J. Guichard, "LQR control for a quadrotor using unit quaternions: modeling and simulation," in *2013 International Conference on Electronics, Communications and Computing*, 2013.